

Three-Dimensional Modeling of Flow and Thermochemical Behavior in a Blast Furnace

YANSONG SHEN, BAOYU GUO, SHENG CHEW, PETER AUSTIN, and AIBING YU

An ironmaking blast furnace (BF) is a complex high-temperature moving bed reactor involving counter-, co- and cross-current flows of gas, liquid and solid, coupled with heat and mass exchange and chemical reactions. Two-dimensional (2D) models were widely used for understanding its internal state in the past. In this paper, a three-dimensional (3D) CFX-based mathematical model is developed for describing the internal state of a BF in terms of multiphase flow and the related thermochemical behavior, as well as process indicators. This model considers the intense interactions between gas, solid and liquid phases, and also their competition for the space. The model is applied to a BF covering from the burden surface at the top to the liquid surface in the hearth, where the raceway cavity is considered explicitly. The results show that the key in-furnace phenomena such as flow/temperature patterns and component distributions of solid, gas and liquid phases can be described and characterized in different regions inside the BF, including the gas and liquids flow circumferentially over the 3D raceway surface. The in-furnace distributions of key performance indicators such as reduction degree and gas utilization can also be predicted. This model offers a cost-effective tool to understand and control the complex BF flow and performance.

DOI: 10.1007/s11663-014-0204-y

© The Minerals, Metals & Materials Society and ASM International 2014

I. INTRODUCTION

THE blast furnace (BF)—basic oxygen furnace process remains the predominant route of steel production, accounting for over 60 pct of global steel output, although the challenges from new ironmaking processes continue. In an integrated steel plant, the ironmaking BF is the main energy consumer, accounting for nearly 70 pct of the whole plant.^[1–3] The practice of a BF is schematically shown in Figure 1, where the solids of coke and ore *etc.* (termed burden) are charged from the furnace top; the high temperature, high velocity air (termed blast) is introduced into the lower part of the furnace *via* tuyeres, forming void zones (termed raceways) and combusts coke to generate reducing gases and smelting heat. As the solids (mainly coke and iron-bearing materials) travel downward and reducing gas goes upward, the latter together with smelting heat reduces and melts the iron-bearing burden to form liquid iron and slag in the so-called cohesive zone. The liquids then percolate through the coke bed (termed as dripping zone) to the hearth. In some cases, the injection of pulverized coal may be practised for operational and

cost benefits.^[4–6] Physically, a modern BF is a high-temperature moving bed reactor, involving counter-, co- and cross-current flows of gas, liquid and solid flows, and heat exchange and chemical reactions.^[1,7] It is very challenging but important to understand the complex in-furnace phenomena of gas–solid–liquid flow and thermochemical behavior, including the circumferential multiphase flow in the vicinity of raceway, and key process indicators, for operational control and optimization in BF practice.

The operation of a BF is usually investigated for two related purposes, *viz.* to predict process indicators and more importantly, to understand internal state of a BF. The two aspects can be studied by different methods including industry-scale investigations, lab/pilot-scale experiments, and mathematical modeling. The industry-scale investigations are normally conducted for measuring the process indicators such as gas utilization rate at furnace top, and for understanding the internal state to a certain degree by means of techniques such as dissection^[8] and tuyere core drilling,^[9] but they are difficult in implementation due to, for example, the need of a BF stoppage and the high cost. Lab/pilot-scale experiments are also used for understanding the internal state of BF operation, for example, by use of an experimental BF in LKAB,^[10] but it cannot estimate the process indicators or cannot fully reflect the in-furnace phenomena of a real large BF, and its cost in terms of maintenance and operation is very high. Because of these aforementioned difficulties, mathematical approach plays a significant role in investigating furnace performance of both predicting process indicators and understanding the internal state, such as a neural network model (or expert system)^[11–13] and/or process

YANSONG SHEN, Research Fellow, and AIBING YU, Professor, are with the Department of Chemical Engineering, Monash University, Clayton, VIC 3800, Australia. Contact e-mail: yansong.shen@monash.edu BAOYU GUO, Research Fellow, is with the School of Materials Science and Engineering, The University of New South Wales, Sydney, NSW 2052, Australia. SHENG CHEW and PETER AUSTIN, Principal Research Engineers, are with the Steelmaking Technology and Planning, BlueScope, PO Box 202, Port Kembla, NSW 2505, Australia.

Manuscript submitted January 16, 2014.

Article published online October 2, 2014.

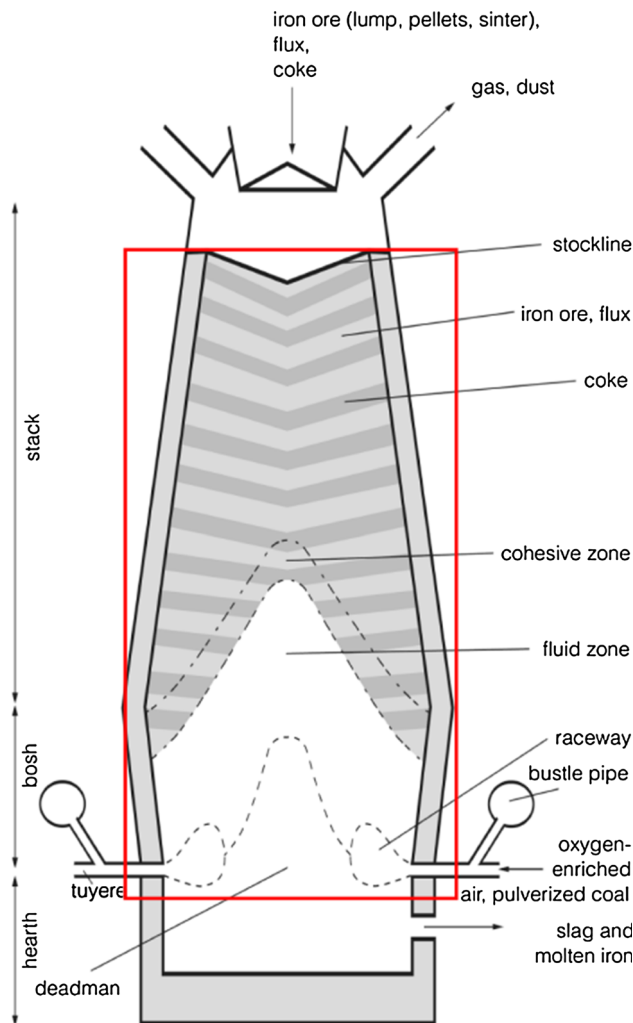


Fig. 1—(Color figure online) Schematic of an ironmaking BF (computational domain of this model is denoted by a red rectangle).

model.^[7,14,15] The former can monitor the furnace operation by handling input and output data including operators' experience and measured data from the furnace but it cannot quantify the in-furnace phenomena in terms of local properties. The latter can predict BF performance indicators, and more importantly provide more detailed understanding of the internal state in a BF, and thus is widely used for understanding and optimizing BF operation.

In a BF process model, the solid and liquid flows may be simulated using different methods. Specifically, solid flow can be simulated using typically two approaches: discrete-based and continuum-based approaches. The discrete-based approach can track and analyse the motion of individual solids and does not need global assumption on the solids,^[16] but it may not be suitable for practical BF simulation, because the number of particles in an actual BF is huge and thus the computational demand is too high for the current computational capability. For this reason, the continuum-based approach, where solid particles are treated as a continuous phase, is the major modeling technique used to describe the internal state of solid flow in a BF. On the

other hand, liquid phase in a BF can be simulated by means of potential flow model,^[17] probability-continuous model,^[18] or force balance model.^[19] The force balance model is considered as the most attractive due to its advantages in computation and representation of the relevant physics of liquid flows in a BF. The above-mentioned techniques for flows of different phases, together with other techniques for heat/mass transfer and chemical reactions, can be incorporated to establish a BF process model, as done by various investigators.^[7,14,15]

The BF process models thus far proposed have been developed largely in 2D and later in 3D, as summarized in the successive reviews by Yagi,^[7] Dong *et al.*^[14] and Ueda *et al.*^[15] These models are mainly implemented with in-house codes. In particular, Yagi and his associates^[7] developed a series of 2D steady-state and later unsteady-state models, and investigated various BF operations, *e.g.*, top gas recycling and charging carbon composite agglomerates.^[20–23] Sugiyama and Sugata^[24] developed a 2D model, known as “BRIGHT” model, focusing on material transfer, reaction and heat transfer in the lumpy zone and cohesive zone. A few off-line sub-models such as burden distribution model (known as RABIT model) were also developed in parallel.^[25] BlueScope (formerly BHP Steel) developed a 2D steady-state numerical model of gas–solid flow in a BF, known as SHAFT model. A sub-model of liquid flow was then incorporated by Chew *et al.*^[19,26] Dong *et al.*^[27] developed a 2D model of gas–solid–liquid flows, where the layered structure of cohesive zone was considered. Recently, Fu *et al.*^[28] also developed a 2D model, focused on the multiphase reacting flow in BF shaft with layered burden. Although these 2D models may reveal the change of furnace indicators under different conditions to a certain degree, 3D modeling and analysis are naturally important for practical BF problems and recommended for simulating the multiphase flow in BFs, especially in the vicinity of the raceway.^[26] To date, only a few 3D BF models have been reported. For example, Takatani *et al.*^[29,30] developed a simplified 3D model and used it to investigate the effects of furnace profile and volume. Their model employs some simplistic assumptions such as vertical constant liquid flow velocity. The 2D model by Yagi^[7] was extended to 3D by de Castro *et al.*^[31,32] for investigating the co-injection of pulverized coal and charcoal in a BF. These models are based on in-house code. They did not consider the raceway explicitly and thus could not reliably describe the 3D features of multiphase flow in the vicinity of the raceway.

In this paper, a 3D model is developed based on the commercial software package ANSYS-CFX to describe the complex behavior of solid–gas–liquid multiphase flow, the heat/mass transfers and chemical reactions in a BF. In the model, the raceway cavity is considered explicitly. The in-furnace phenomena can be simulated and described comprehensively including multiphase flow/temperature patterns and component concentrations. In particular, the 3D features of circumferential flow and maldistribution in the vicinity of the raceway are characterized in details. The in-furnace distributions

Table I. Governing Equations Used in this BF Model

Aspect	Governing Equations
Mass	$\nabla \cdot (\varepsilon_i \rho_i \mathbf{U}_i) = S_i$
Momentum	
Gas	$\nabla \cdot (\varepsilon_g \rho_g \mathbf{U}_g \mathbf{U}_g) = \nabla \cdot \boldsymbol{\tau}_g - \varepsilon_g \nabla p + \rho_g \varepsilon_g \mathbf{g} + \mathbf{f}_g^s + \mathbf{f}_g^{l,d}$
Solid	$\nabla \cdot (\varepsilon_s \rho_s \mathbf{U}_s \mathbf{U}_s) = \nabla \cdot \boldsymbol{\tau}_s - \varepsilon_s \nabla p_s + \rho_s \varepsilon_s \mathbf{g}$
Liquid	$\mathbf{f}_{l,d}^g + \mathbf{f}_{l,d}^s + \varepsilon_{l,d} \rho_l \mathbf{g} = 0$
Heat and species	$\nabla \cdot (\varepsilon_i \rho_i \mathbf{U}_i \phi_{i,m}) - \nabla \cdot (\varepsilon_i \Gamma_i \nabla \phi_{i,m}) = S_{\phi_{i,m}}$
Volume fraction	$\varepsilon_s + \varepsilon_g + \varepsilon_l = 1$
State equation for gas phase	$p = \sum_i (y_i M_i) RT_g / V_g$

where $S_i = -\sum_k \beta_{i,k} R_k^*$, $\boldsymbol{\tau}_i = \varepsilon_i \mu_i [\nabla \mathbf{U}_i + (\nabla \mathbf{U}_i)^T] - 2/3 \varepsilon_i \mu_i (\nabla \cdot \mathbf{U}_i) \mathbf{I}$; if $\phi_{i,m}$ is $H_{i,m}$, $\Gamma_i = \frac{k_i}{c_{p,i}}$, $S_{\phi_{i,m}} = \delta_{ij} h_{ij} \alpha (T_i - T_j) + c_{p,i} T_i \delta_i \sum_k \beta_{k,i} R_k^* + \eta_i \sum_k R_k^* (-\Delta H_k)$; if $\phi_{i,m}$ is $\omega_{i,m}$, $\Gamma_i = \rho_i D_i$, $S_{\phi_{i,m}} = \sum_k \alpha_{i,m,k} R_k^*$; $\phi_{i,m} = \omega_{g,CO} + \omega_{g,CO_2} + \omega_{s,Fe_2O_3} + \omega_{s,Fe_3O_4} + \omega_{s,FeO} + \omega_{s,flux}$.

Table II. Empirical Correlations for the Interaction Forces Between Phases

Phases	Interaction Forces	Ref.
Gas–solid	$\mathbf{f}_g^s = -\mathbf{f}_s^g = -\left(\alpha_f \rho_g \mathbf{U}_g^s + \beta_f\right) \mathbf{U}_g^s$	Dong <i>et al.</i> ^[14]
Gas–liquid	$\mathbf{f}_g^{l,d} = -\mathbf{f}_{l,d}^g = -\left(\frac{h_{l,d}}{d_l} + \frac{A_{sl,d}}{6}\right) \left[150 \left(\frac{\varepsilon_s + h_{l1}}{d_w}\right) \mu_g + 1.75 \rho_g \mathbf{U}_g \right] \frac{\mathbf{U}_g}{\varepsilon_g}$	Chew <i>et al.</i> ^[19]
Liquid–solid	$\mathbf{f}_{l,d}^s = \left(\frac{150}{36} \mu_l \frac{A_{sl,d}^2}{h_{l,d}^2} + \frac{1.75}{6} \rho_l \frac{A_{sl,d}}{h_{l,d}} \mathbf{U}_l \right) \mathbf{U}_l$	Chew <i>et al.</i> ^[19]

where $d_l = \max\{d_{l,g}, d_{l,h}\}$; $d_{l,g} = \left[\max\left\{-6.828 \text{sign}(\sqrt{X_p} - 0.891)(\sqrt{X_p} - 0.891)^2, 0\right\} + 0.695\right] / \sqrt{\rho_l g / \sigma}$.
 $d_{l,h} = \left[\max\left\{6.828 \text{sign}(f_1)(f_1)^2, 0\right\} + 0.695\right] / \sqrt{\rho_l g / \sigma}$; $f_1 = \left[\max\left\{\ln(h_{l,t}/h_{l,t0}), 0\right\} / 0.513\right]^{1/2.642} - 0.891$.
 $X_p = \Delta p_e / (\Delta x \rho_l g) \left\{\rho_l g \varphi^2 d_s^2 / \sigma / \varepsilon_s^2\right\}^{0.3} (1 + \cos \theta)^{-0.5}$.

Table III. Empirical Correlations for Different Inter-phase Heat Transfers

Phases	Inter-phase Heat Transfer	Ref.
Gas–solid	$h_{gs} = r Nu k_g / d_p$, $Nu = 2.0 + 0.6 (Pr_g)^{0.333} (9 Re_g)^{0.5}$	Omori ^[1]
Gas–liquid	Ranz–Marshall model	Ranz <i>et al.</i> ^[47]
Liquid–solid	$h_{ls} = r k_l / d_p \left(\frac{2 \sqrt{Re_s Pr_s}}{1.55 \sqrt{Pr_s} + 3.09 \sqrt{0.372 - 0.15 Pr_s}}\right)$	Austin <i>et al.</i> ^[20]

of key performance indicators of a BF such as reduction degree and gas utilization are also predicted.

II. NUMERICAL MODELING

In this section, the governing equations used in the simulation are described firstly. Then the inter-phase interactions in aspect of force, heat/mass transfer and chemical reactions, together with the treatments of solid/liquid flows and cohesive zone, are outlined. Finally, the solution procedure of this CFX-based model is described.

A. Governing Equations

The proposed BF model is a 3D steady-state model, extending from the burden surface at the throat down to

the liquid surface in the hearth. It considers three phases, namely, gas, solid and liquid, as they dominate the performance of the furnace when pulverized coal injection is not practised or when limited unburnt coal enters the BF from the raceway. These phases are treated as continuous phases and modelled by means of different methods. Specifically, the solids (coke and iron ore) are described using the so-called viscous model.^[20] The gas phase flow is described by the well-established Navier–Stokes equations through porous media using the well-established Ergun equation. The liquids (hot metal and slag) are modelled by the so-called force balance approach,^[19,33] where the liquid is treated as a single phase under the influence of gravity force, gas drag force and bed resistance force. The sum of the three forces is equal to zero at steady state. The properties of the liquid phase are determined as the weighted averages of two liquids in terms of mass fractions. Each phase is

Table IV. Reaction Rate of Key Chemical Reactions Considered in the Model

Reaction	Reaction Rate	Ref.
$\text{Fe}_2\text{O}_{3(s)} + 3\text{CO}_{(g)} \rightarrow 2\text{Fe}_{(s)} + 3\text{CO}_{2(g)}$	$R_1 = \frac{N_{\text{ore}} \pi d_{\text{ore}}^2 \phi_{\text{ore}}^{-1} \rho_g [K/(1+K)] [\xi_{\text{co}} - \xi_{\text{CO}_2} / K (M_{\text{CO}} / M_{\text{CO}_2})]}{k_r^{-1} + 0.5 d_{\text{ore}} [(1-f_s)^{-1/3} - 1] D_j^{-1} + [(1-f)^{2/3} k_1 (1+1/K)]^{-1}}$	Omori ^[1]
$\text{FeO}_{(l)} + \text{C}_{(s)} \rightarrow \text{Fe}_{(l)} + \text{CO}_{(g)}$	$R_2 = k_2 A_c / (V_b a_{\text{FeO}})$	Omori ^[1]
$\text{CO}_{2(g)} + \text{C}_{(s)} \rightarrow 2\text{CO}_{(g)}$	$R_3 = f(d_{\text{coke}}) h(S_L) \frac{E_f \rho_s \xi_{\text{coke}} \bar{M}_g}{3600 M_{\text{coke}}} \frac{k_1 p_T \xi_{\text{CO}_2}}{1 + p_T (k_2 y_{\text{CO}_2} + k_3 y_{\text{CO}} + k_5 y_{\text{H}_2\text{O}})}$	Hatano <i>et al.</i> ^[48]
$\text{FeO}_{(s)} \rightarrow \text{FeO}_{(l)}$	$R_4 = \left\langle \frac{T_i - T_{\text{min,sm}}}{T_{\text{max,sm}} - T_{\text{min,sm}}} \right\rangle_0 \frac{\int_0^1 \xi_{\text{sm}} U_i \rho_i \epsilon_i dA}{M_{\text{sm}} \text{Vol}_{\text{cell}}}$	Austin <i>et al.</i> ^[38]

Table V. Treatment of Cohesive Zone Used in the Study

Parameters	Treatment
Solid volume fraction	$\epsilon_s = \xi_{\text{ore}} \epsilon_{\text{ore}} + \xi_{\text{coke}} \epsilon_{\text{coke}}$
Solid particle size	$d_s = (\xi_{\text{ore}} / d_{\text{ore}} + \xi_{\text{coke}} / d_{\text{coke}})^{-1}$
Solid heat conductivity	$k_s = (\xi_{\text{ore}} / k_{\text{ore}} + \xi_{\text{coke}} / k_{\text{coke}})^{-1}$
Gas flow resistance in cohesive zone	vertical direction to the burden: $\alpha_f = \xi_{\text{ore}} \alpha_{\text{ore}} + \xi_{\text{coke}} \alpha_{\text{coke}}; \beta_f = \xi_{\text{ore}} \beta_{\text{ore}} + \xi_{\text{coke}} \beta_{\text{coke}}$ radial direction to the burden: $\alpha_f = (\xi_{\text{ore}} / \sqrt{\alpha_{\text{ore}}} + \xi_{\text{coke}} / \sqrt{\alpha_{\text{coke}}})^{-2}; \beta_f = (\xi_{\text{ore}} / \beta_{\text{ore}} + v / \beta_{\text{coke}})^{-1}$

composed of various chemical species, as listed below. In addition, the total volume fraction shared by the three phases sums to unity. The governing equations describing the gas–solid–liquid flows are listed in Table I. In this study, steady-state modeling is conducted due to the fact that the motion of solid flow is much slower than other flows and the relevant heat and mass transfers.

B. Inter-phase Momentum/Heat Transfers and Chemical Reactions

The interactions between solid, gas and liquid phases are intense in aspects of momentum and heat. The sub-models used in the past are adopted in this study to simulate these interactions. Thus, gas–solid heat transfer coefficient, h_{gs} , is obtained from a modified Ranz–Marshall correlation,^[1,34]

$$h_{\text{gs}} \gamma \text{Nu} k_g / d_p, \text{Nu} = 2.0 + 0.6(\text{Pr}_g)^{0.333} (9\text{Re}_g)^{0.5},$$

where Nu is the Nusselt number for flow in a packed bed, and γ is an empirical correction faction introduced to account for bed movement and fusion, given by.

$$\gamma = 0.2 - 0.18 \min \left(1.0, \max \left(0, \frac{T_s - 1473}{200} \right) \right).$$

The inter-phase heat transfer coefficients between gas and liquid and between solid and liquid are available in the literature.^[1] The empirical correlations used in this model for calculating the inter-phase momentum and heat transfers between the three phases are summarized in Tables II and III, respectively. The key chemical reactions considered in this model include direct and indirect reduction of iron ore by coke and CO, solution loss and melting of FeO and flux. Since the verification

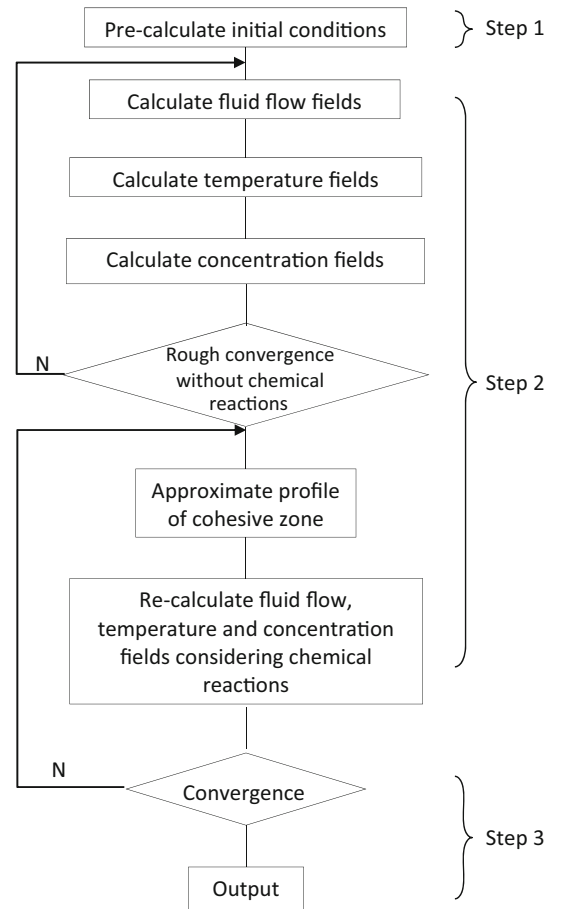


Fig. 2—Solution procedure of the model.

of chemical reactions is beyond the current study, the expressions used to calculate the reaction rates are based on the previous models of BF, as listed in Table IV. The

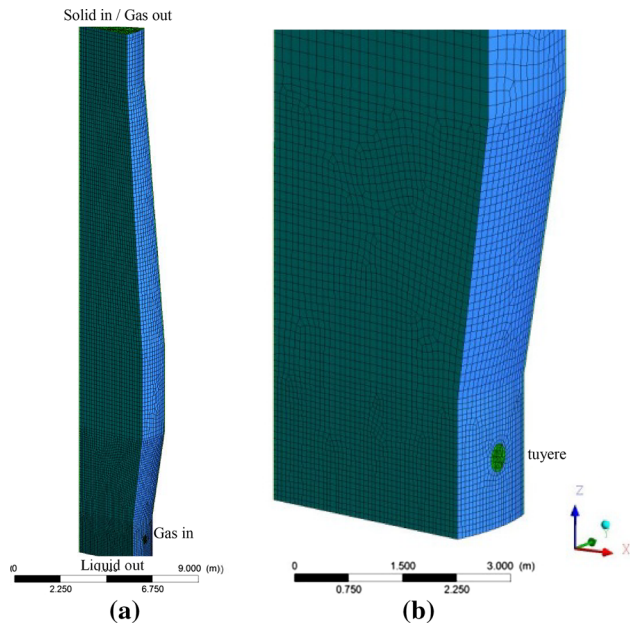


Fig. 3—Computational domain with inlet/outlet conditions indicated for each phase: (a), whole domain and (b), enlarged view of the lower part of BF.

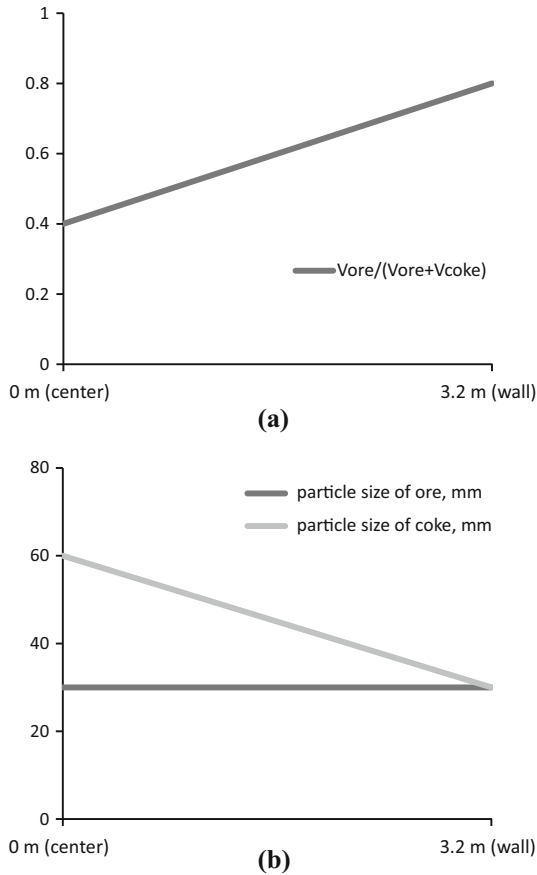


Fig. 4—Burden distribution of the simulated BF: (a), volume ratio of ore in solid charging and (b), particle size of ore and coke.

Table VI. Simulation Conditions and Operational Conditions Used in the Model

Operational Conditions	Variables and Values
Gas	
Gas rate at a tuyere ($\text{kg m}^{-2} \text{s}^{-1}$)	11.7
Volume flux ($\text{Nm}^3 \text{tHM}^{-1}$)	1511
Inlet gas components (molar pct)	34.95 CO; 65.05 N_2
Inlet gas temperature [K ($^{\circ}\text{C}$)]	2313 (2040)
Top pressure (atm)	2.0
Solid	
Solid rate at furnace top ($\text{kg m}^{-2} \text{s}^{-1}$)	1.22
Ore (t tHM^{-1})	1.64
Ore components (mass fraction)	Fe_2O_3 0.656; FeO 0.157
Ave. ore particle size (m)	0.03
Coke (t tHM^{-1})	0.5023
Coke components (mass fraction)	C 1.0
Ore voidage	$0.403(100d_{\text{ore}})^{0.14}$
Coke voidage	$0.153 \log d_{\text{coke}} + 0.724$
Ave. ore/(ore + coke) volume ratio	0.5923
Liquid	
Components (mass fraction)	C 0.04; Fe 0.9509
Density (kg m^{-3})	6600
Viscosity ($\text{kg m}^{-1} \text{s}^{-1}$)	0.005
Conductivity ($\text{W m}^{-1} \text{K}^{-1}$)	28.44
Surface tension (N m^{-1})	1.1
Slag rate (t tHM^{-1})	0.377
Density (kg m^{-3})	2600
Viscosity ($\text{kg m}^{-1} \text{s}^{-1}$)	1.0
Conductivity ($\text{W m}^{-1} \text{K}^{-1}$)	0.57
Surface tension (N m^{-1})	0.47

hydrogen content and its reactions are neglected in the simulation. It is noted that rather than “manual” extraction used in the past,^[27] the coke consumption rate in the BF is naturally determined by the reactions considered in the model. This is considered as another improvement compared to our previous model.^[27] In the previous BF models, the solid loading on the furnace top is usually fixed, thus independent of chemical reactions considered. For this reason, coke consumption in the raceway has to be treated by manually exacting all remaining coke particles out of tuyere to meet the overall mass balance. In this study, the coke consumption is determined by the chemical reactions considered in the model, and the solid loading at the furnace top is directly related to the chemical reactions. Specifically, the raceway region and the combustion reaction in the region are modelled based on: (i) the raceway region is assumed as a fixed sphere-shaped cavity and (ii) the coke combustion of $2\text{C} + \text{O}_2 = 2\text{CO}$ is modelled implicitly with conserved mass and enthalpy, although it is implemented only in the blast inlet surface. On the other hand, to be computationally efficient, as mentioned above, this model does not explicitly model the layered cohesive zone, as an approach used in most of the reported BF models.

C. Other Treatments Used in This Model

In addition to the governing equations of solid, gas and liquid phases and their interactions, some treat-



Fig. 5—Boundaries of cohesive zone determined by the simulation.

ments are also employed in the modeling of BF process. They are outlined below.

1. Solid-liquid flows

The treatments of the solid and liquid phases are summarized as follows. Solid particles form the dominant phase in BF. The solid particles of ore and coke are charged from the furnace top with a uniform downward velocity. The layered structure is determined by the burden distribution at the furnace top and also the timelines of solid flow.^[35,36] Specifically, during solids descent, the particle properties at the top of the furnace are transported to other parts of the furnace along the solid streamlines so as to initialize particle size and porosity distributions throughout the furnace. After identifying the cohesive zone, dripping zone and deadman, the properties of these regions are recalculated. Specifically, in the cohesive zone, iron-bearing materials are still treated as part of the solid phase, characterized by porosity and particle size. In the dripping zone, bed permeability is calculated based on coke particles only. In the deadman, coke particle size is assumed to be

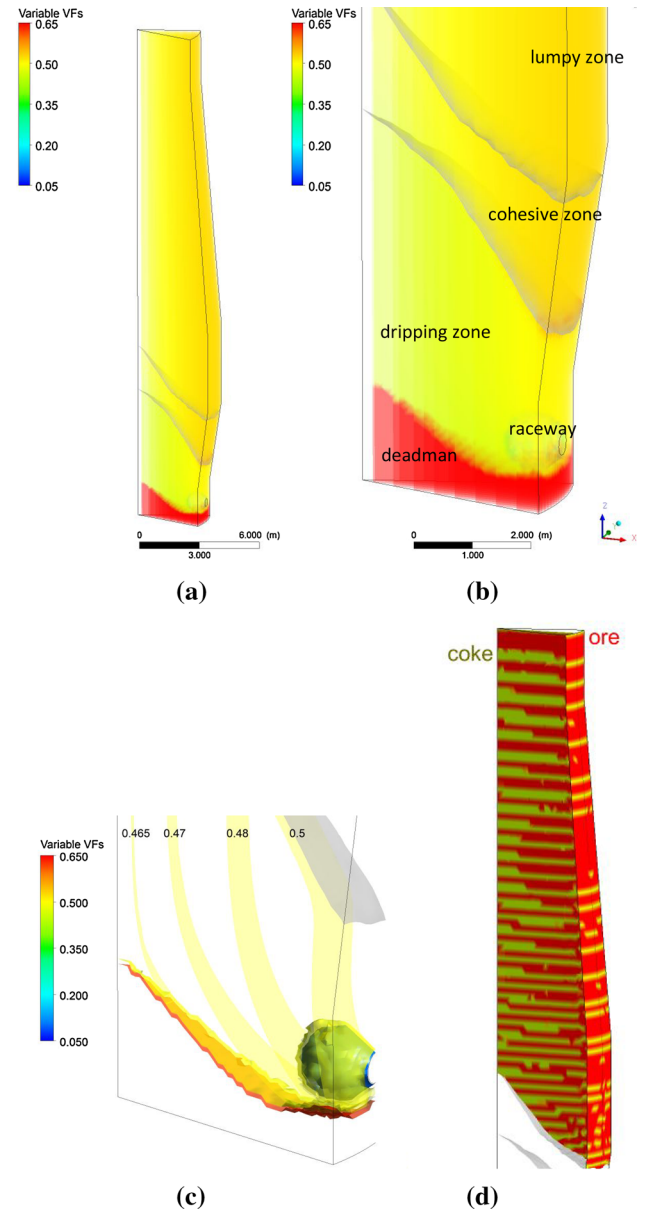


Fig. 6—(Color figure online) Volume fraction of solid phase: (a), over the whole domain; (b), enlarged view in the lower part of furnace; (c), over the localised iso-surfaces in the half raceway and (d), burden distributions of coke (green) and ore (red) in the stack of furnace.

0.02 m and solid volume fraction is 0.65. The position and profile of deadman surface is prescribed by a solid iso-velocity curve, which is determined by an approach as used by Zhang *et al.*^[36] Beyond the iso-velocity curve, particles move with a velocity less than a critical value—one-ninth of the particle diameter per minute in this study. Once specified, the deadman will behave like a motionless object, and its profile will be treated as a boundary to the moving particles, in conjunction with walls, inlet and outlet, in the determination of the velocity fields. On the other hand, liquids, *i.e.*, hot metal and slag, play a critical role in the lower part of BF. They carry mass and energy while redistributing gas flow, and in turn may be redistributed at the lower part of BF. Inclusion of liquid flow into the BF

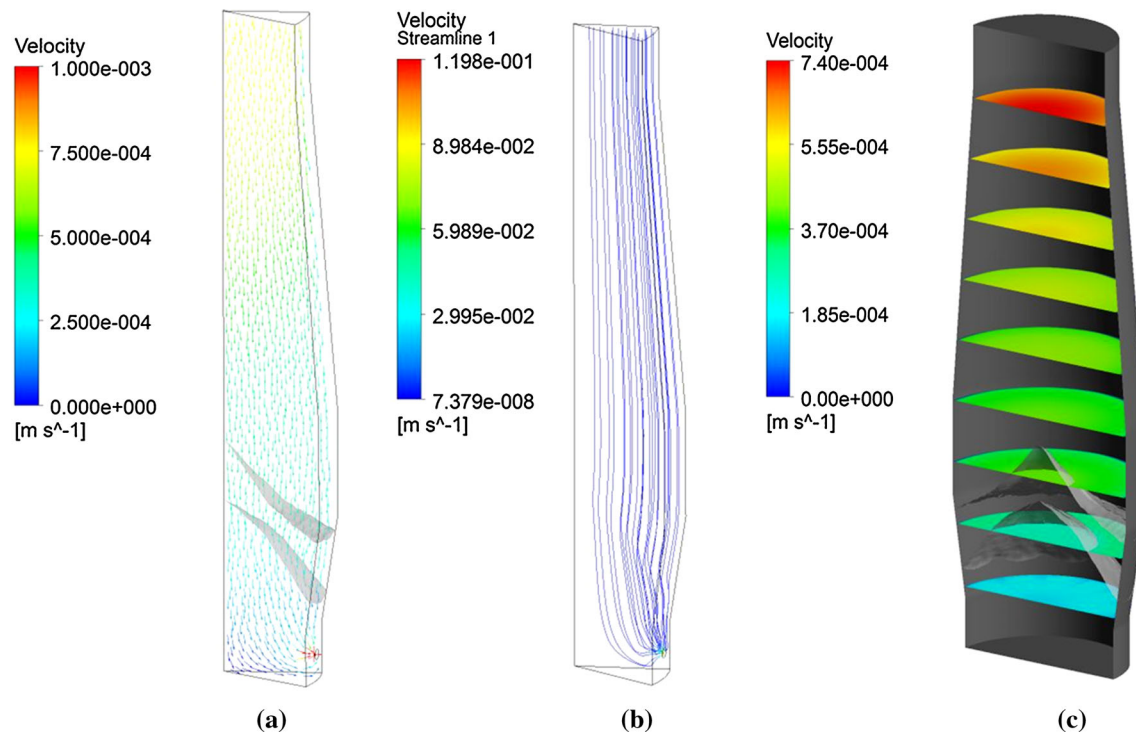


Fig. 7—Flow pattern of solid phase: (a), velocity vector; (b), streamline and (c), contours on horizontal slices at different heights.

model will improve the prediction of other operational variables such as gas temperature in the lower part of BF. In this study, the main treatments of liquid phase are consistent with those proposed by Chew *et al.*^[26] The liquids are thus treated as droplets or rivulets, which will achieve a steady average percolation velocity quickly based on gas, liquid and packing properties considering the interactions between liquid, gas and solid phases. The liquids are generated inside the cohesive zone with a flow rate as a function of total amount of liquid, inlet area and ore/coke ratio. In the dripping zone, the liquids are considered with reference to the moving coke bed, where static holdup carries liquids through the lower zone of BF; the force balance on dynamic holdup is superimposed on the coke velocity field; and liquid holdups are calculated as a function of coke physical properties.

2. Cohesive zone

The shape and position of cohesive zone are the collected results of solid–gas flow, heat transfer and chemical reactions. In turn, the cohesive zone will impact the permeability, fluid flow, gas utilization, thermal and chemical efficiency and hot metal quality in the furnace. In this work, numerically, the cohesive zone is presumed to lie between the solid temperature (T_s) isotherms at 1473 K and 1673 K (1200 °C and 1400 °C). It should be noted that T_s refers to as the solid phase temperature, even for the solids that are in the melting state. Shrinkage ratio, Sh_r , defined as the ratio of the decreased volume to the original volume occupied by iron ore, is usually used to present the softening and melting changes of iron-bearing materials to modify the ore layer resistance.^[37] In this study, the normalized shrinkage ratio Sh_r^* is adopted to determine the particle

size and porosity of iron-bearing materials inside the cohesive zone, which results from flow and heat/mass transfers of all reactions.^[27] The cohesive zone can be treated as isotropic, anisotropic non-layered or layered structures, respectively.^[27] Following the previous studies,^[7,14,15] the anisotropic treatment is adopted in this model. That is, the cohesive zone is treated as a mixed region of iron ore and coke particles with different properties in the vertical and radial directions to the burden. Thus, the anisotropic treatment corresponds to the operation with layered charging but a small batch weight for coke and iron-bearing materials.^[27] Table V outlines the anisotropic treatment of cohesive zone.

D. Numerical Techniques

The conservation equations and other equations/expressions listed above can be solved by an in-house code, or commercial CFD code such as CFX or Fluent. In this study, different from the previous models based on in-house codes,^[7,27,29,38] the model is based on the framework of the commercial software package—ANSYS-CFX v12.0. Specifically, the Eulerian multicomponent–multiphase module is used in this model. This platform is chosen for easy transfer due to better readability and potential connections with our previous CFX-based sub-models such as raceway^[6,39,40] and hearth,^[41,42] and other existing sub-models such as burden distribution.^[43] As shown in Figure 2, the solution procedure employed in this model involves the following steps:

- Step 1: Before CFX runs, a pre-calculation of the mass balance is conducted for determining the

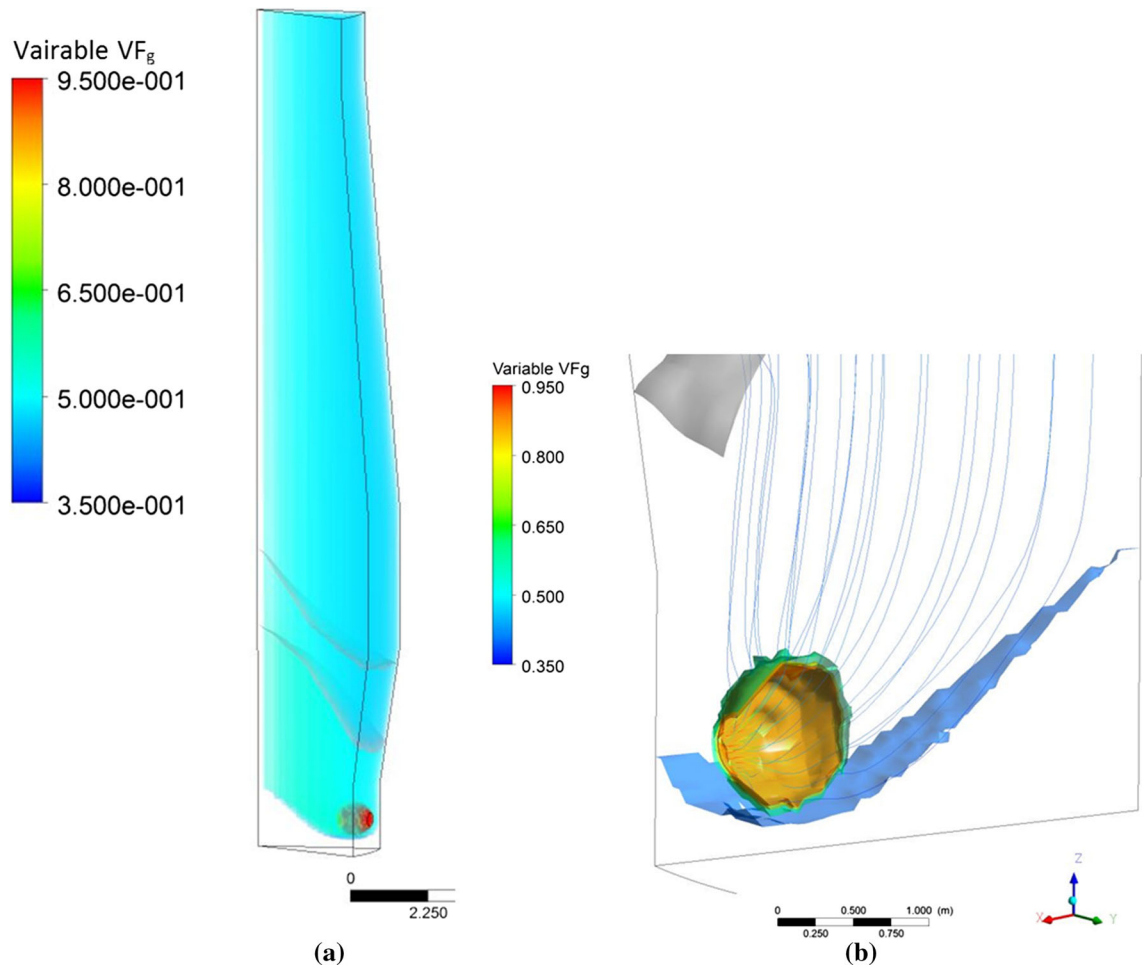


Fig. 8—Volume fraction of gas phase: (a), over the whole domain and (b), over the localised iso-surfaces in the half raceway.

boundary and initial conditions in terms of solid–gas–liquid flow, temperature and concentration fields;

- Step 2: The respective CFX runs for solid, gas and liquid phases are conducted for calculating their flow-thermal-chemical behavior. Initially, chemical reactions are not considered for rough convergence, and an approximate profile of cohesive zone is estimated preliminarily. Then chemical reactions are considered and solid–gas–liquid flow, temperature and concentration fields will be recalculated for determining the profile of cohesive zone. The inlet condition of gas at the tuyere is fixed as the pre-set initial condition, *i.e.*, gas rate, whereas the inlet conditions of solids at the furnace top, *i.e.*, solid rate, are dependent on the result in the last update of a shared library (which is created and used outside of CFX runs for interphase coupling, with the updating done *via* repeating the above calculations for the respective phases);
- Step 3: The convergence will be reached when the relative difference in cohesive zone positions predicted by two consecutive iterations is less than 10 pct (not 10 pct of the whole furnace height). In the meantime, other more strict CFD convergence in aspects of momentum, heat and mass transfers of solid–gas–liquid phases, are all required for this BF model, so

that the imbalance of the solid, gas and liquid phases in terms of mass, momentum, energy, concentrations, pressure *etc.*, are less than 1 pct. It is noted that separate CFX runs plus interphase coupling *via* a library used in this study is largely for better stability towards convergence.

E. Simulation Conditions

The computational domain covers the stack part and bosh part of the BF, from burden surface to hearth liquid surface. The model is applied to a BF of around 1000 m³ inner volume with height 25 m, throat diameter 6.4 m, belly diameter 8.8 m and hearth diameter 7.2 m. Considering the symmetrical distribution of process variables, a half of BF is used in a 3D geometry covering an arc of 30 deg, meaning 12 tuyeres are assumed in this simulation. A spherical cavity (1.0 m in diameter) adjunct to the tuyere inlet is assumed to simulate the raceway. The geometry and mesh are illustrated in Figure 3. The mesh of the computational domain includes 46,390 nodes and 46,547 elements. The sensitivity of the results to different mesh sizes is also examined, confirming the mesh independence.

The burden distribution and particle sizes at the furnace top are assumed as input conditions, as illustrated in Figure 4. The volume ratio of ore/(ore + coke) is assumed to change linearly from 0.4 at the furnace center to 0.8 at the wall; the ore particle size is assumed to be constant at 30 mm whereas coke particle size is assumed to change linearly from 60 mm at the center to 30 mm at the wall. It is noted that the ore/coke ratio is low at the furnace center, and coke particle size is small near the furnace wall. This burden distribution provides high permeability at the furnace center due to large particles causing large voids for fluid flow. The burden distribution is assumed, as the measurements of such data are not available. The burden distribution will then vary as solids travel downward, resulting from various inter-phase interactions with gas-liquid flows and chemical reactions, as discussed in Section II-C. The top pressure is assumed to be 2 atm in the simulation. Other main simulation conditions of operating data used in this study are listed in Table VI. The physical and chemical properties of each component in the three phases can be found elsewhere.^[27]

III. RESULTS AND DISCUSSION

In this section, the typical internal state of a BF is discussed in terms of flow and thermochemical behavior of gas, solid and liquid phases, and key process performance indicators such as reduction degree and gas utilization. In particular, in addition to the overall in-furnace phenomena, the multiphase flow in the vicinity of the raceway is characterized in detail, where the 3D-featured circumferential flow and maldistribution are more evident. The 3D distributions of process variables in the BF can be visualized comprehensively on the slices and also by a new view—volume rendering, for better illustration of some variables. The volume rendering enables visualizing field variables throughout the entire domain by varying both transparency and colour of a plot as a function of a variable value, that is, higher transparency in blue means lower value of a variable.

A. Solid-Gas-Liquid Flow Patterns

1. Cohesive zone

The location and shape of cohesive zone is the collected results of multiphase flow, heat and mass transfer. Figure 5 shows the location and shape of the cohesive zone in a half of the BF. The location and shape of the cohesive zone is visualized using two surfaces, which are defined by the solid temperatures of 1473 K (1200 °C) for upper boundary of cohesive zone and 1673 K (1400 °C) for lower boundary of cohesive zone, respectively. The simulations indicate that the cohesive zone in the shape of inverse V is obtained in the lower part of the BF. It is largely uniform and slightly thicker at the two ends of cohesive zone, which was also observed in References 1, 47.

2. Solid phase

Figure 6 shows the volume fraction of solid phase (VF_s). The volume fraction is generally lower in the

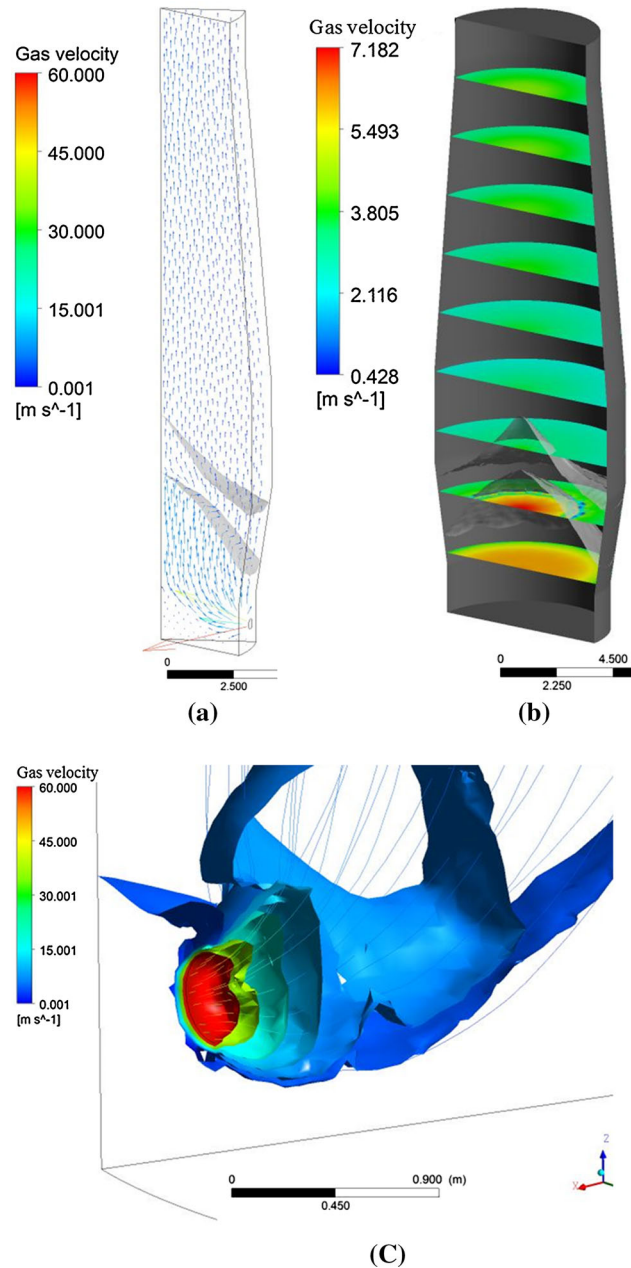


Fig. 9—Flow pattern of gas velocity: (a), along the central vertical plane; (b), contour on horizontal slices at different heights and (c), over the localised iso-surfaces of gas velocity.

furnace center, resulting from the assumed burden distribution (Figure 4), but it varies in different zones inside the BF. First, in the lumpy and dripping zones, the permeability is higher at the furnace center than near the wall in the radial direction. Secondly, inside the inverted V-shaped cohesive zone, the volume fraction is gradually decreased from upper boundary to lower boundary due to the phase change from iron ore to liquid iron. Thirdly, in the raceway region, a sphere-shaped region is very low in solid volume fraction, nearly zero, as assumed in the initial conditions. The 3D features around the raceway are observed. For example, the iso-surfaces of solid volume fractions, e.g., 0.46 to

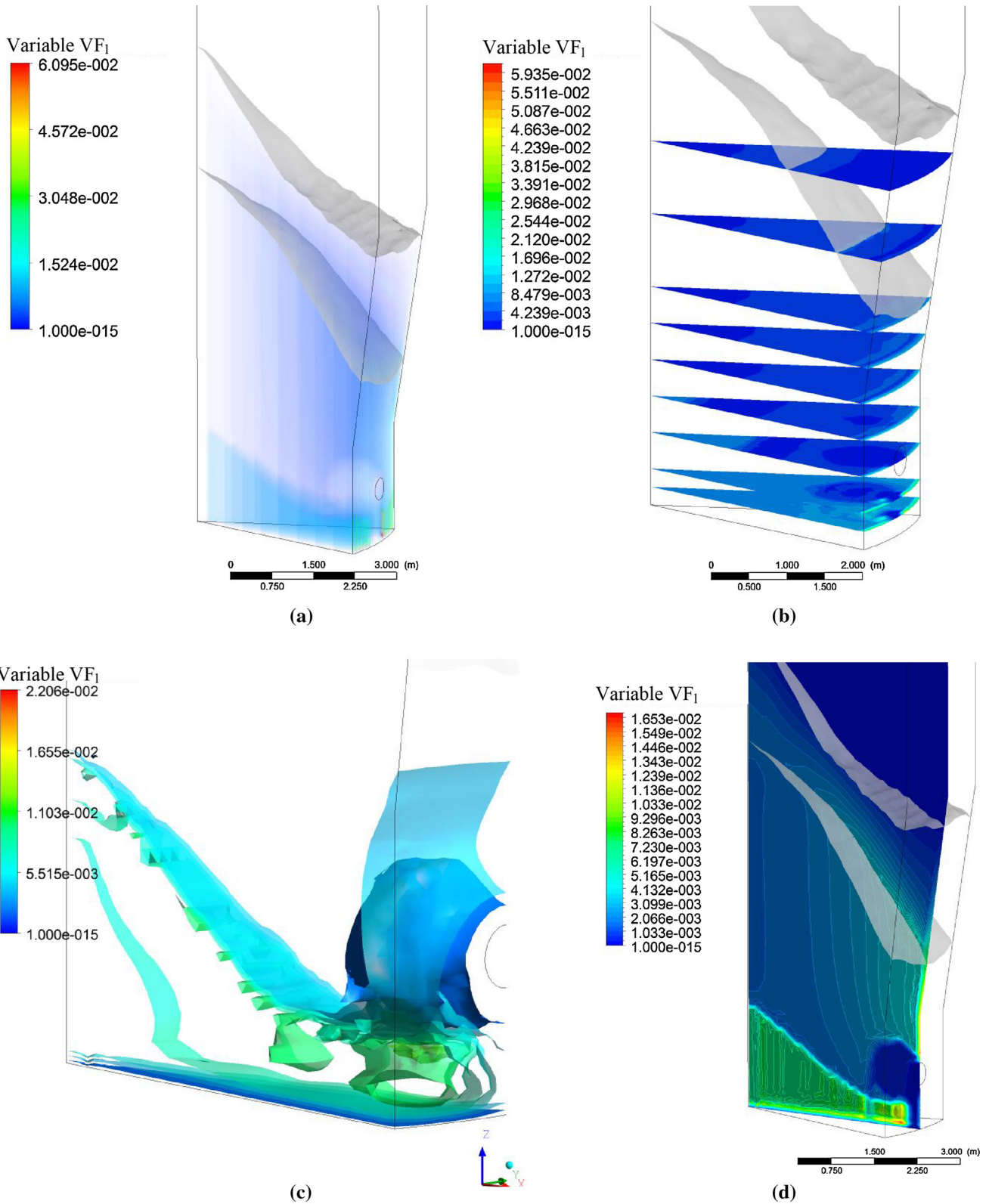


Fig. 10—Volume fraction of liquid phase: (a), rendered over the working volume; (b), contour on horizontal slices at different heights; (c), over the localised iso-surfaces in the vicinity of the raceway and (d), along the central vertical plane.

0.5, are almost spherical in shape, leading to the rapid decrease of porosity from nearly 1.0 to ~ 0.5 over the raceway surface. Fourthly, in the deadman region, the

volume fraction is assumed to be much higher, ~ 0.65 , meaning much lower permeability. In addition, the solids of coke and iron ore are also envisaged according

to the timeline of solids in Figure 6(d) and the layered structure is not explicitly considered in this model, where more coke is found at the furnace center above the cohesive zone.

Figure 7 shows the flow fields of solid phase inside the BF in terms of velocity vectors, streamline and contours on horizontal slices at different heights. Generally, the solid downward velocity is slightly slower near the furnace wall, compared to that at the center (Figure 7(c)). In the lumpy zone, the solid downward velocity is gradually reduced. After entering the cohesive zone, the solid downward velocity is rapidly decreased and the directions are deflected, because coke particles have to fill the space occupied by the iron ore, which transforms from solid to liquid phase. Compared to the lumpy zone, the solid downward velocity in the dripping zone is much slower because the solid flow in the dripping zone is only driven by the coke consumption in the lower part of the furnace. The deadman region is formed at the center bottom due to solid movement and coke consumption in the raceway. As a result, the solid velocity is directed towards the raceway bottom at an extremely slow speed. Near the raceway and tuyere, relatively fast solid velocity vectors are observed. The deviations were also observed in References 27, 44 and explained as a result from the plug flow conditions where raceway or tuyere acts as the outlet for the solid phase.

3. Gas phase

Figure 8 shows the volume fraction of gas phase (VF_g). It can be observed that the volume fraction of gas is generally slightly higher in the furnace center. This radial variation pattern is observed from top to cohesive zone corresponding to the solid flow and distribution (Figure 6). Compared to the lumpy zone, the gas volume fraction in the dripping zone is lower, but still has a similar radial pattern variation pattern. In the raceway region, *i.e.*, the sphere-shaped region, the circumferential gas flow is observed. The gas volume fraction in the raceway is very high, nearly 1.0. In the deadman region, the volume fraction of gas is only 0.35, meaning a very low permeability for gas flow.

Figure 9 shows the gas velocity field in the furnace. It can be observed that after blasted into the furnace *via* tuyeres at a high speed, the gas reduces its speed gradually inside the raceway. After reaching the raceway boundary, gas streams slow down rapidly, and penetrate not only from the raceway end along the tuyere direction but also from the raceway surface. This is also evidenced by the 3D iso-surfaces of gas velocities and volume fractions (Figures 8(b) and 9(c)). Then the gas travels very slowly in the deadman region due to the low permeability and has to travel over the deadman surface, then flow upward in the dripping zone. In the dripping zone, the gas flow is at a higher speed near the center than near the wall. After reaching the lower boundary of the cohesive zone, the upward velocity is decreased, with directions deflected. Compared to the dripping zone, the gas velocity in the lumpy zone is lower due to the increase in gas density as the gas cools. In the lumpy zone, the gas velocity is gradually

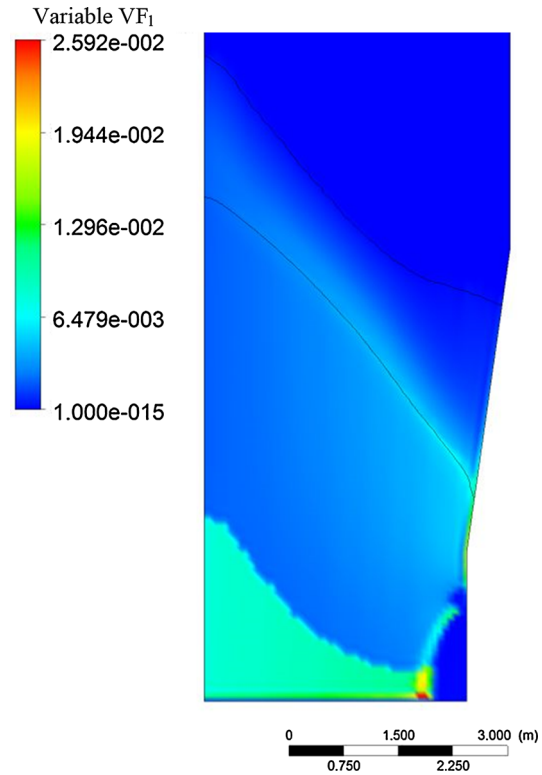


Fig. 11—Liquid flow pattern predicted by a 2D slot model.

decreased and generally higher at the furnace center (Figure 9(b)). It is noted that the 3D features of gas flow, *e.g.*, flow through the side of raceway (Figure 8(b)), and iso-surfaces of gas velocity inside the raceway, are not predictable in the past 2D BF models.

4. Liquid phase

In this 3D model, a sphere-shaped raceway is assumed for simplicity. Figure 10 shows the volume fraction of liquid phase (VF_l) in views of 3D volume rendering, along slices, and iso-surfaces, so as to describe the liquid flow comprehensively, especially in the vicinity of the raceway. Clearly, liquid distribution varies significantly in different zones below the cohesive zone. Liquids are generated inside the inverted V-shaped cohesive zone from the softening/melting of ferrous materials, but the quantity varies in the radial direction, *i.e.*, higher liquid generation near the wall mainly because of the higher ore/coke ratio near the wall side, an input condition for the present study. In the dripping zone, the volume fraction of liquid is different in the radial direction, *i.e.*, lower in the furnace center. This is because, in addition to more liquid generation near the wall, higher center permeability allowing for more gas flow near the center and more liquids flow near the wall also contributes to this feature. Compared to the dripping zone, the volume fraction of liquid is higher in the deadman due to the low solid porosity, slower solid/liquid velocity and then higher liquid holdup. The liquid volume fraction in the raceway is nearly zero, meaning that liquid does not enter the raceway. Instead, the liquids' flow is circumferential, *i.e.*, over the entire raceway surface through

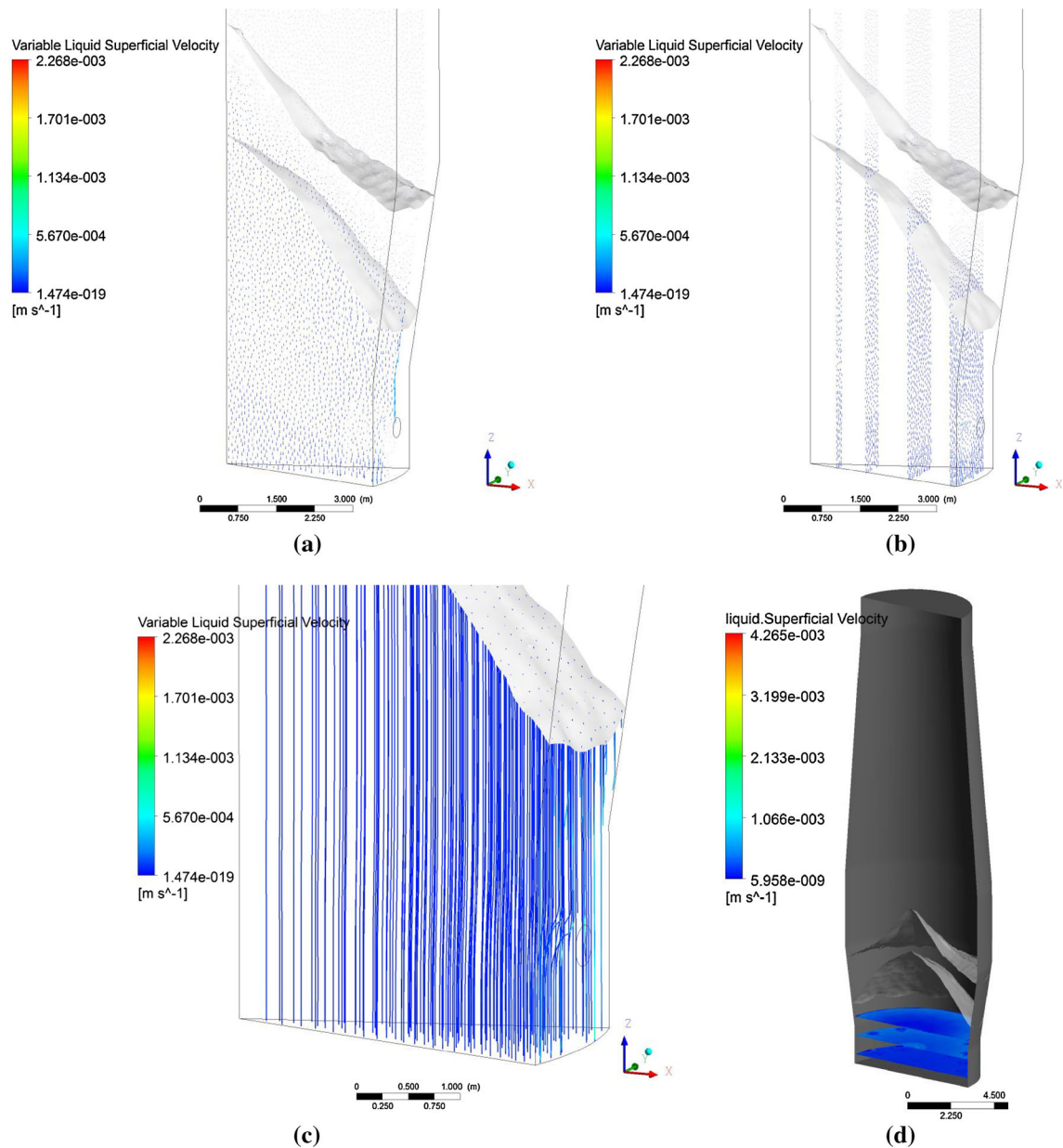


Fig. 12—Flow pattern of liquid phase: (a), vectors along the middle plane (X - Z); (b), vectors along four parallel planes (Y - Z); (c), streamlines of liquid phase and (d), distribution on the radial slices.

the pores of the surrounding coke bed, leading to a peak liquids volume fraction below the raceway cavity (Figure 10(c)). This is because liquids are pushed away around the sphere-shaped raceway surface by strong gas-liquid interaction at the raceway boundary. They then flow through the porous media of the surrounding coke bed due to the balanced gas-liquid-solid force interaction, resulting in high liquid flux between raceways. Solids travel over the deadman surface towards the bottom of the raceway (Figure 7(b)), entraining liquids to the area below the raceway to a certain degree. Also liquids are generated inside the cohesive zone and flow in the dripping zone near the wall. As a result, liquid accumulation is also observed below the raceway. For these reasons, a ‘dry’ sphere-shaped raceway can be

identified (Figure 10(c)). Therefore, the liquids, carrying mass and heat, will impair and redistribute the gas flow and also can be redistributed by the prevailing gas and packing properties radially and circumferentially during descent to the hearth.

In the past, 2D slot modeling without raceway cavity was widely used for simulating the internal state of BF.^[20,22,26,27,44] Prior to developing the current 3D model, a similar 2D slot model was also developed for describing the liquid flow, where liquids are deflected along the radial direction only, leading to a prominent liquid stream located at a certain distance from the tuyere (Figure 11). This is also observed in the previous 2D studies.^[26,27] Such a result is regarded as compromised due to the geometric limitation of the 2D slot

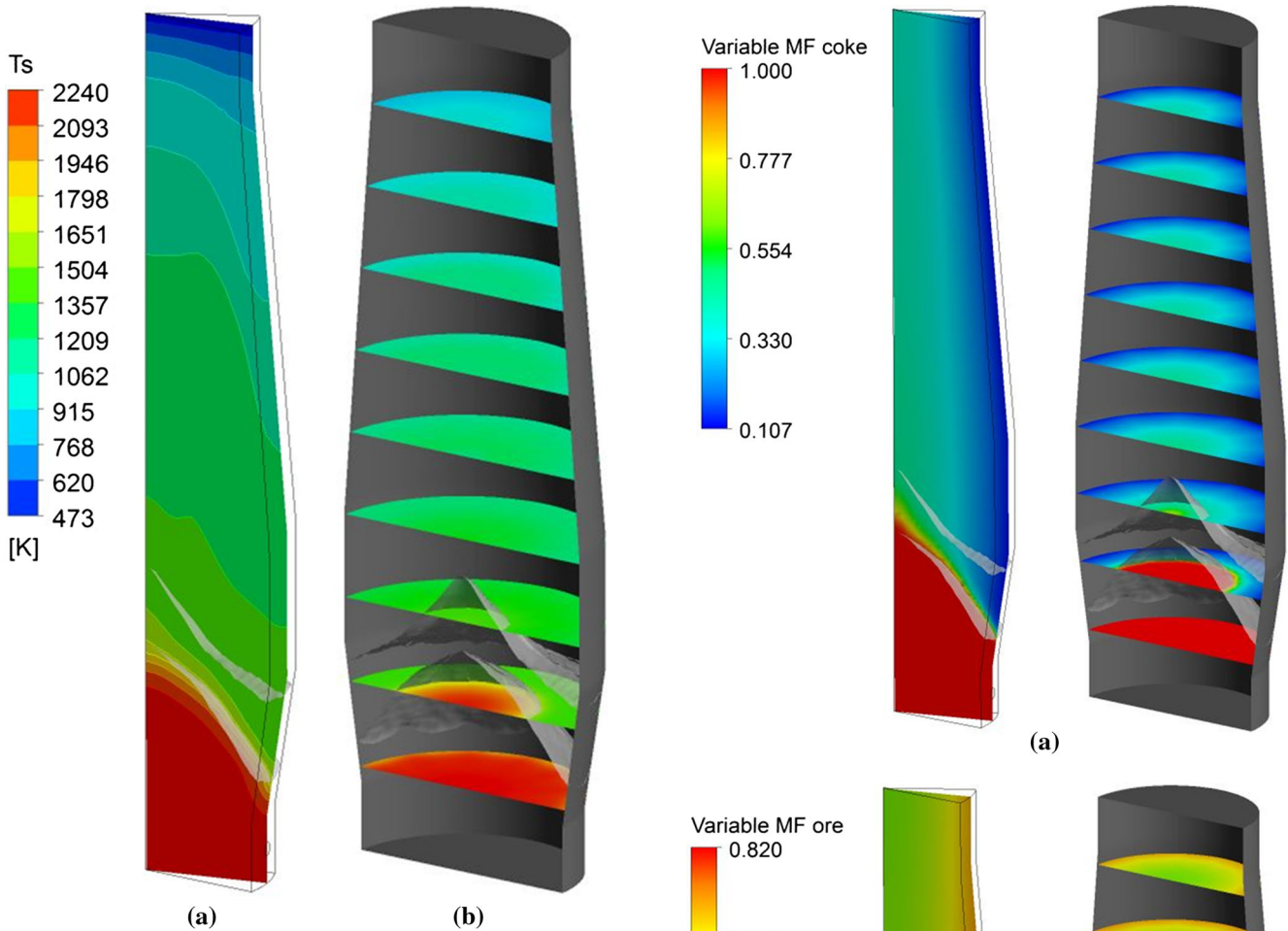


Fig. 13—Temperature field of solid phase: (a), at the central vertical plane and (b), contour on horizontal slices at different heights.

model and cannot fully reflect the liquid flow in a practical BF where the raceway is a 3D cavity. However, in this 3D study, where the raceway cavity is explicitly considered and volume fraction of liquid is explicitly solved in the governing equations, the liquid flow is found to be quite different from those predicted by the previous 2D slot model. That is, near the tuyere, the liquids predicted by this model flow largely in the vicinity of the raceway, *i.e.*, over the raceway surface (Figure 10(c)) with liquid accumulation and flux between the raceway cavities. Therefore, the 3D model with raceway cavity will predict a notably different liquid flow pattern and should be used in numerical studies where the localised liquid flow pattern near the raceway is the concern.

Figure 12 shows the flow patterns of liquid phase below the cohesive zone by means of superficial velocity vectors (a&b), streamline (c) and distribution on the slices (d). It is observed that liquid velocity is generally higher near the furnace wall than the center. This is also the case in the previous models.^[31] Inside the cohesive zone, the liquid downward velocity is gradually increased. The liquid droplets then percolate through the

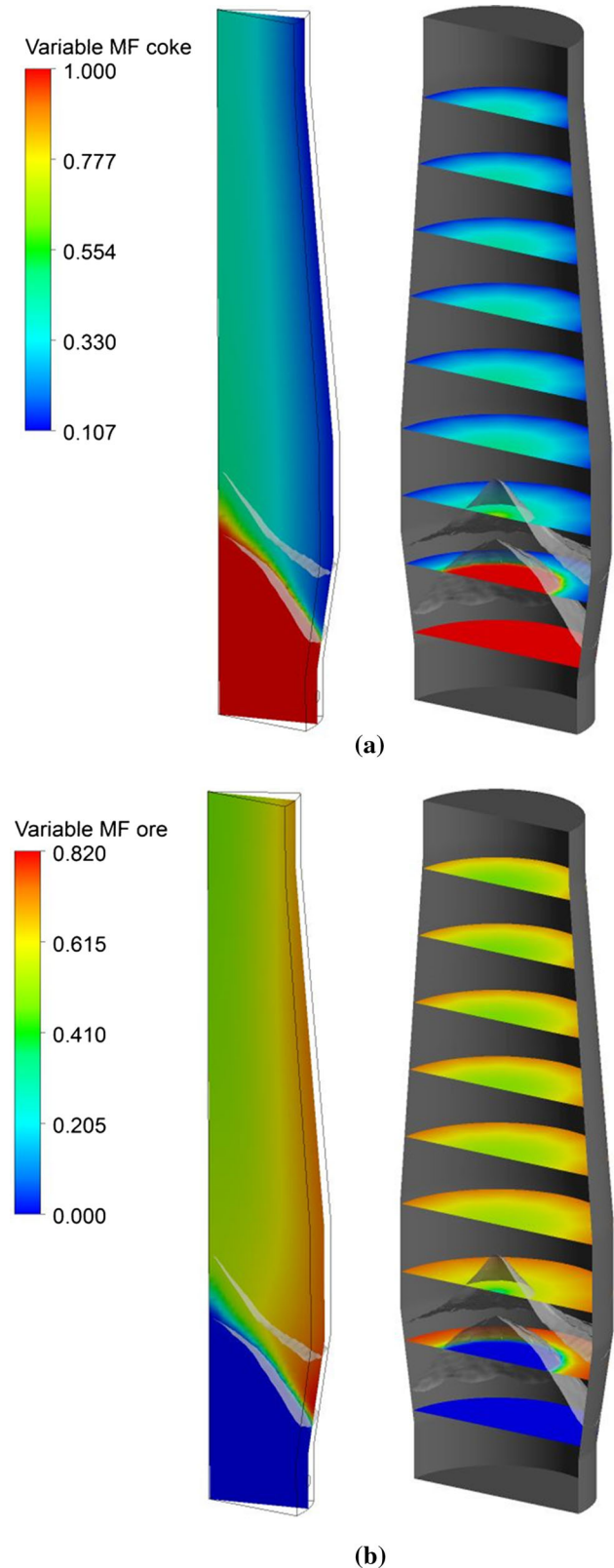


Fig. 14—Distributions of mass fractions of solid components in the solid phase: at the central vertical plane (left) and contour on horizontal slices at different heights (right): (a), coke and (b), ferrous materials.

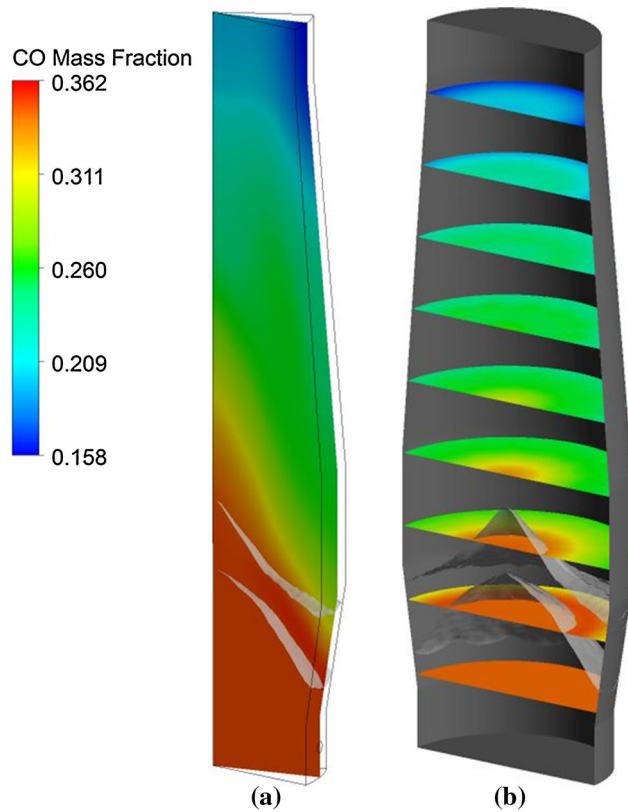


Fig. 15—Distribution of CO mass fraction in the BF: (a), at the central vertical plane and (b), contour on horizontal slices at different heights.

coke bed in the dripping zone almost vertically. In addition to the descending flow of liquids in the dripping zone and deadman region, liquid flow is deflected in the vicinity of the raceway (Figure 12(c)), due to the strong gas–liquid–solid interactions. A region of low liquid speed can be observed along the raceway boundary (Figure 12(b)), although the liquid volume fraction there is extremely low (Figure 10). In this study, the hot metal and slag are treated as one single liquid phase for simplification. As a result, the general features of liquid flow can be characterized in the regions above the hearth surface. The respective liquid flows of hot metal and slag in the hearth have been simulated using a separate model^[41,42] and can be integrated into this 3D BF process model. This will be done in the future.

B. Thermochemical Behavior and Process Performance Indicators

1. Solid temperature

Figure 13 shows the solid temperature along the central vertical plane and on horizontal slices at different heights. It is observed that the solid temperature is generally higher near the furnace center (Figure 13(b)), because more coke particles are charged at the furnace center, allowing more gas flow of higher temperature and thus higher solid temperature in the center. In the lumpy zone, the solids are quickly heated up at the furnace top and then during descent, the solids are

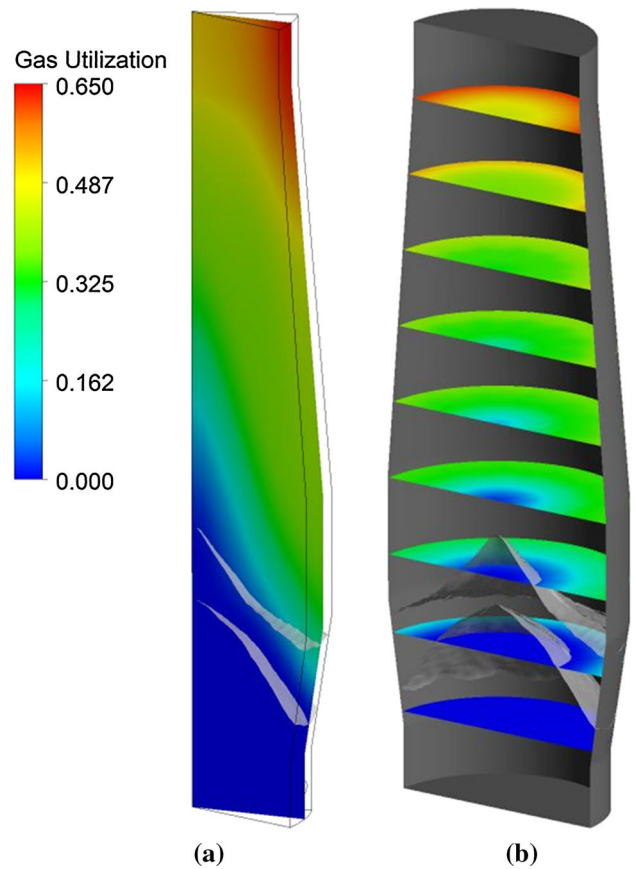


Fig. 16—Distribution of gas utilization: (a), at the central vertical plane and (b), on the horizontal slices at different heights.

gradually heated up. The solid temperature is increased rapidly inside the cohesive zone, especially near the lower boundaries of the cohesive zone. Compared to the lumpy zone and cohesive zone, the dripping zone shows much higher solid temperature clearly due to the continued heat transfer from the hotter gas close to the raceway. In the dripping zone, the solid temperature is higher in the center than near the wall because of higher permeability and gas flow (Figure 9) combined with the lower heat demand for reduction and solution loss reactions associated with the low ore volume fraction, providing heat and leading to higher temperatures. In contrast, liquids of relatively low temperature mainly travel near the wall (Figure 10), removing heat and leading to low solids temperature compared to the center. In the vicinity of the raceway, some 3D features can also be captured such as higher temperature within the raceway than between the raceways (Figure 13(b)). The temperature of gas/liquid phases is qualitatively similar to that of solid phase in the different zones, because solid phase is a slow moving bed, and there is strong heat transfer between solid, gas and liquid phases.

2. Solid components

Figure 14 shows the mass fractions of the two solid components: coke particles and iron-bearing materials in the solid phase. It is observed that more coke particles

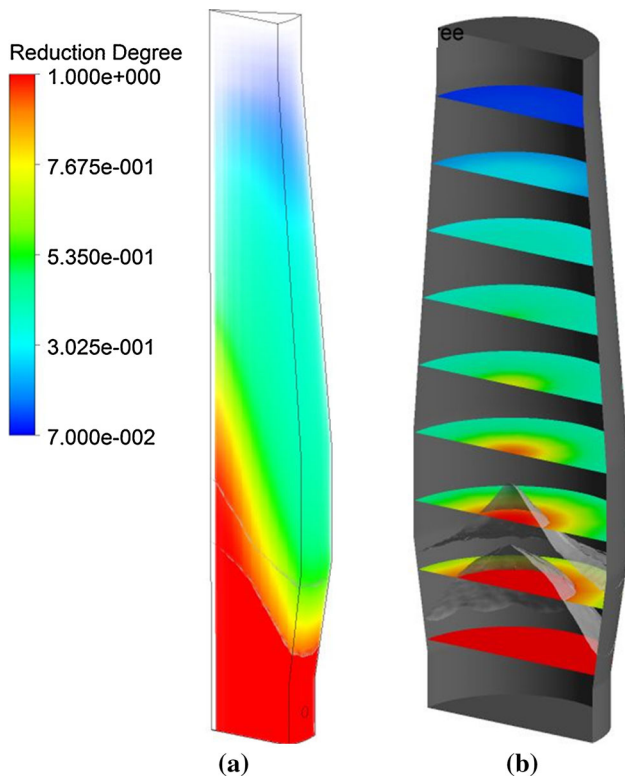


Fig. 17—Distribution of the degree of reduction of ore: (a), rendered over the working volume and (b), contour on horizontal slices at different heights.

and less iron-bearing materials are found at the furnace center, consistent with the assumed burden distribution (Figure 4). As solids descend in the lumpy zone, the mass fractions of coke and ferrous materials change slightly. Inside the cohesive zone, particularly near the lower boundary of cohesive zone, the ferrous materials are quickly consumed, being reduced and melted into liquids of iron and slag. As a result, below the cohesive zone, the mass fraction of ferrous solids is zero and coke particles fully represent the solid phase.

3. Gas distribution

Figure 15 shows the distribution of CO mass fraction in the BF. It is observed that CO concentration is generally high near the furnace center due to the high permeability and lower ore/coke ratio there (Figure 15(b)). Below the cohesive zone, the CO concentration does not change significantly from its tuyere inlet value due to regeneration by the solution loss reaction. After passing the cohesive zone, during gas ascent, the CO is gradually consumed in the lumpy zone as a result of strong indirect reduction reactions. It is noted that the sudden change of CO concentration is not aligned with the upper boundary of cohesive zone. This is because of the preferential gas flow and low ore/coke ratio in the center, leading to sustained regeneration and less CO consumption in the center.

4. Gas utilization

Gas utilization is an important performance indicator representing the energy efficiency in the furnace to a

certain degree. It is defined as the percentage of CO₂ in the CO and CO₂ gas (volume fraction), *i.e.*,

$$\text{Gas utilization} = \frac{\text{CO}_2}{\text{CO}_2 + \text{CO}}$$

Figure 16 shows the distribution of gas utilization from the lower part to furnace top. It is observed that the distribution of gas utilization is generally higher near the furnace wall (Figure 16(b)) due to the assumed higher ore/coke ratio near the furnace wall. Below the cohesive zone, the gas utilization is zero, as CO₂ is not stable in this region. After reaching the cohesive zone, a sudden change is observed, but this change does not fully match the profile of the cohesive zone, *i.e.*, a delayed sudden increase near the furnace center because the prevailing gas flow is observed in the furnace center. Then the gas utilization is gradually increased in the lumpy zone due to the strong indirect reduction reaction. In addition, the gas utilization can also be calculated at the furnace top. In this case, the averaged gas utilization on the furnace top is 57 pct.

5. Reduction degree

Figure 17 shows the distribution of the degree of reduction of ore from the BF top to bottom. It is observed that the reduction degree is generally high at the furnace center (Figure 17(b)) due to the high availability of reducing gas in this region. The reduction degree then varies in different zones. In the lumpy zone, the reduction degree is gradually increased from zero to around 0.5 upon reaching the cohesive zone. In the cohesive zone, the reduction degree is increased rapidly, where an early increase is observed near the furnace center due to the preferential gas flow and high coke/ore ratio. After passing the cohesive zone, the ore is fully reduced to liquid iron, meaning 100 pct reduction degree. Such in-furnace distributions of process indicators, *e.g.*, gas utilization and reduction degree, can represent the collected results of flow and thermochemical behaviors at the different zones of BF in response to changes of BF operation, and thus provide guidance for process optimization.

IV. CONCLUSIONS

A 3D CFX-based model has been developed to describe the complex behavior of multiphase flow, heat/mass transfer and chemical reactions in a BF. The model is applied to a BF covering from the burden surface at the top to the liquid surface in the hearth. In this model, the 3D raceway cavity is considered explicitly, allowing for detailed description of multiphase flows in the vicinity of the raceway. The results show that the in-furnace phenomena of flow and thermochemical behavior of solid–gas–liquid phases can be characterized in terms of velocity, volume fraction, temperature and component distributions, respectively. Process performance indicators can also be obtained. The key findings are summarized below:

1. In general, the control of burden and hence permeability distribution is important. This is evidenced by the simulated results for the BF considered, where the furnace center shows higher bed permeability due to the assumed burden distribution, leading to higher temperature, lower liquid volume fraction but higher gas volume fraction, higher reduction degree and lower gas utilization.
2. The in-furnace phenomena vary in different zones such as lumpy zone, cohesive zone, dripping zone, deadman and raceway. Many process variables change significantly in the cohesive zone. Compared to the cohesive zone and dripping zone, the lumpy zone shows higher solid velocities/lower gas velocities, much lower temperature, and higher gas utilization and lower reduction degree. As solids descend, coke mass fraction is rapidly increased; the CO concentration is rapidly decreased as gas ascends. Below the cohesive zone, the deadman zone shows much lower solid/gas velocities compared to the dripping zone. The liquids are redistributed by the prevailing gas and packing properties in the radial direction during descent to the hearth.
3. The 3D circumferential gas-liquid flows in the vicinity of the raceway have been depicted. The liquid flow pattern predicted by this 3D model is different from that predicted by the previous 2D slot model. The former predicts liquid flow circumferentially around the 3D raceway surface through the pores of the surrounding coke bed, whereas the latter predicts a prominent liquid stream located some distance from the tuyere only as a compromised result from the 2D limitation.

The model provides a cost-effective tool for understanding the internal state of a BF and also sets up a platform for linking with other sub-models, *e.g.*, raceway^[39,45,46] and hearth.^[41,42] It can be used for investigating the effects of operational changes on furnace performance and identifying methods to improve energy efficiency of a BF, and the results will be reported in the future publications.

ACKNOWLEDGMENTS

The authors are grateful to the Australian Research Council and BlueScope for the financial support of this work, and to Dr X.F. Dong and Dr D. Pinson of BlueScope for valuable discussion.

NOMENCLATURE

a_{FeO}	Activity of molten wustite
A_c	Effective surface area of coke for reaction (m^2)
$A_{\text{sl,d}}$	Effective contact area between solid and liquid in unit volume of bed ($\text{m}^2 \text{m}^{-3}$)

c_p	Specific heat ($\text{J kg}^{-1} \text{K}^{-1}$)
d	Diameter of solid particle (m)
d^*	Normalized particle size ($d^* = d/d_{\text{max}}$)
$d_{\text{l,g}}$	Liquid droplet diameter as affected by gas flow (m)
$d_{\text{l,h}}$	Droplet diameter as affected by holdup (m)
d_w	Effective packing diameter (m)
D	Diffusion coefficient ($\text{m}^2 \text{s}^{-1}$)
$D_{\text{g,n}}^e$	Effective diffusivity of component n , $n = \text{CO}$ ($\text{m}^2 \text{s}^{-1}$)
E_f	Effectiveness factors of solution loss reaction
f_s	Degree of reduction
\mathbf{f}	Interaction force per unit volume ($\text{kg m}^{-2} \text{s}^{-2}$)
$f(d_{\text{coke}}) h(S_L)$	Correction factors for particle size and coke reactivity
\mathbf{g}	Gravitational acceleration (m s^{-2})
h	Holdup
$h_{\text{l,t}}$	Total holdup
h_{ij}	Heat transfer coefficient between i and j phase ($\text{W m}^{-2} \text{K}^{-1}$)
H	Enthalpy (J kg^{-1})
k	Thermal conductivity ($\text{W m}^{-1} \text{K}^{-1}$)
k_f	Gas-film mass transfer coefficient (m s^{-1})
k_i	Rate constant of i th chemical reactions ($i = 1, 2, \text{ or } 3$) (m s^{-1})
K	Equilibrium constant
M_i	Molar mass of i th species in gas phase (kg mol^{-1})
\bar{M}_g	Molar mass of gas mixture (kg mol^{-1})
N_{ore}	Number of ore particles per unit volume of bed (m^{-3})
p	Pressure (Pa)
Pr	Prandtl number
R	Gas constant ($8.314 \text{ J K}^{-1} \text{ mol}^{-1}$)
R^*	Reaction rate ($\text{mol m}^{-3} \text{ s}^{-1}$)
Re	Reynolds number
S	Source term
Sh_r^*	Normalized shrinkage ratio, $Sh_r^* = Sh_r/Sh_{r,\text{max}}$, $Sh_{r,\text{max}} = 0.7$
T	Temperature (K)
\mathbf{U}	True velocity (m s^{-1})
V_b	Bed volume (m^3)
V_g	Gas volume (m^3)
Vol_{cell}	Volume of control volume (m^3)
X_p	Dimensionless pressure drop
y_i	Mole fraction of i th species in gas phase

GREEK SYMBOLS

Γ	Diffusion coefficient
\mathbf{I}	Identity tensor
ϕ	General variable
φ	Shape factor
α	Specific surface area ($\text{m}^{-2} \text{m}^{-3}$)

α_f, β_f	Coefficients in Ergun Eq.
β	Mass increase coefficient of fluid phase associated with reactions (kg mol^{-1})
δ	Distribution coefficient
ε	Volume fraction
θ	Contact angle (deg)
η	Fractional acquisition of reaction heat
μ	Viscosity ($\text{kg m}^{-1} \text{s}^{-1}$)
ρ	Density (kg m^{-3})
σ	Surface tension (N m^{-1})
τ	Stress tensor (Pa)
ω	Mass fraction
$\xi_{\text{ore}}, \xi_{\text{coke}}$	Local ore, coke volume fraction
ξ_i	Mass fraction of species i
γ	Scaling factor for convective heat transfer

SUBSCRIPTS

e	Effective
g	Gas
i	Identifier (g, s or l)
i, m	m th species in i phase
j	Identifier (g, s or l)
k	k th reaction
l	Liquid
l,d	Dynamic liquid
s	Solid
sm	FeO or flux in solid phase

SUPERSCRIPTS

e	Effective
g	Gas
l,d	Dynamic liquid
s	Solid
T	Total

REFERENCES

1. Y. Omori: *Blast Furnace Phenomena and Modelling*, Elsevier, London, 1987.
2. A. Orth, N. Anastasijevic, and H. Eichberger: *Miner. Eng.*, 2007, vol. 20, pp. 854–61.
3. F.M. Shen, X. Jiang, G.S. Wu, G. Wei, X.G. Li, and Y.S. Shen: *ISIJ Int.*, 2006, vol. 46, pp. 65–69.
4. Y.S. Shen, B.Y. Guo, A.B. Yu, and P. Zulli: *Fuel*, 2009, vol. 88, pp. 255–63.
5. Y.S. Shen, A.B. Yu, and P. Zulli: *Steel Res. Int.*, 2011, vol. 82, pp. 532–42.
6. Y.S. Shen, D. Maldonado, B.Y. Guo, A.B. Yu, P. Austin, and P. Zulli: *Ind. Eng. Chem. Res.*, 2009, vol. 48, pp. 10314–23.
7. J. Yagi: *ISIJ Int.*, 1993, vol. 33, pp. 619–39.
8. K. Kanbara, T. Hagiwara, A. Shigemitsu, S.I. Kondo, Y. Kanayama, K.I. Wakabayashi, and N. Hiramoto: *Trans. Iron Steel Inst. Jpn.*, 1977, vol. 17, pp. 371–80.
9. R.R. Willmers: *Revue De Metallurgie-Cahiers D*, 1992, vol. 89, pp. 241–49.
10. G.Q. Zuo and H. Mats: *J. Iron. Steel Res. Int.*, 2009, vol. 16, pp. 1166–71.
11. X.J. Hao, F.M. Shen, G. Du, Y.S. Shen, and Z. Xie: *Steel Res. Int.*, 2005, vol. 76, pp. 694–99.
12. X.G. Bi, L.C. Fu, W. Xiong, and Y. Jin: *J. Iron. Steel Res. Int.*, 2009, vol. 16, pp. 914–22.
13. G.Q. Zuo, J.T. Ma, and B. Bjorkman: *Steel Res.*, 1998, vol. 69, pp. 41–48.
14. X.F. Dong, A.B. Yu, J.I. Yagi, and P. Zulli: *ISIJ Int.*, 2007, vol. 47, pp. 1553–70.
15. S. Ueda, S. Natsui, H. Nogami, J. Yagi, and T. Ariyama: *ISIJ Int.*, 2010, vol. 50, pp. 914–23.
16. Z.Y. Zhou and A.B. Yu: *Prog. Comput. Fluid Dyn.*, 2004, vol. 4, pp. 39–45.
17. J. Szekeley and Y. Kajiwara: *Trans. Iron Steel Inst. Jpn.*, 1979, vol. 19, pp. 76–84.
18. J. Wang, R. Takahashi, and J. Yagi: *Tetsu to Hagane*, 1991, vol. 77, pp. 1585–92.
19. S.J. Chew, P. Zulli, and A.B. Yu: *ISIJ Int.*, 2001, vol. 41, pp. 1112–21.
20. P.R. Austin, H. Nogami, and J. Yagi: *ISIJ Int.*, 1997, vol. 37, pp. 458–67.
21. J.A. de Castro, H. Nogami, and J. Yagi: *ISIJ Int.*, 2000, vol. 40, pp. 637–46.
22. K. Yang, S. Choi, J. Chung, and J. Yagi: *ISIJ Int.*, 2010, vol. 50, pp. 972–80.
23. M.S. Chu, H. Nogami, and J. Yagi: *ISIJ Int.*, 2004, vol. 44, pp. 2159–67.
24. T. Sugiyama and M. Sugata: *Seitetsu Kenkyu*, 1987, vol. 325, pp. 34–43.
25. S. Matsuzaki, T. Nishimura, A. Shinotake, K. Kunitomo, M. Naito, and T. Sugiyama: *Nippon Steel Tech. Rep.*, 2006, vol. 94, pp. 87–95.
26. S.J. Chew, P. Zulli, and A.B. Yu: *ISIJ Int.*, 2001, vol. 41, pp. 1122–30.
27. X.F. Dong, A.B. Yu, S.J. Chew, and P. Zulli: *Metall. Mater. Trans. B*, 2010, vol. 41B, pp. 330–49.
28. D. Fu, Y. Chen, Y. Zhao, J. D'Alessio, K.J. Ferron, and C.Q. Zhou: *Appl. Therm. Eng.*, 2014, vol. 66, pp. 298–308.
29. K. Takatani, T. Inada, and Y. Ujisawa: *ISIJ Int.*, 1999, vol. 39, pp. 15–22.
30. T. Inada, K. Takata, K. Takatani, and T. Yamamoto: *ISIJ Int.*, 2003, vol. 43, pp. 1003–10.
31. J.A. de Castro, H. Nogami, and J. Yagi: *ISIJ Int.*, 2002, vol. 42, pp. 44–52.
32. J.A. De Castro, A.J. Da Silva, Y. Sasaki, and J. Yagi: *ISIJ Int.*, 2011, vol. 51, pp. 748–58.
33. G.X. Wang, S.J. Chew, A.B. Yu, and P. Zulli: *Metall. Mater. Trans. B*, 1997, vol. 28B, pp. 333–43.
34. M. Hatano and K. Kurita: *Trans. Iron Steel Inst. Jpn.*, 1982, vol. 22, pp. 448–56.
35. S.J. Zhang, A.B. Yu, P. Zulli, B. Wright, and P. Austin: *Appl. Math. Model.*, 2002, vol. 26, pp. 141–54.
36. S.J. Zhang, A.B. Yu, P. Zulli, B. Wright, and U. Tuzun: *ISIJ Int.*, 1998, vol. 38, pp. 1311–19.
37. T. Sugiyama, T. Sato, M. Nakamura, and Y. Hara: *Tetsu to Hagane*, 1980, vol. 66, p. 1908.
38. P.R. Austin, H. Nogami, and J. Yagi: *ISIJ Int.*, 1997, vol. 37, pp. 748–55.
39. Y.S. Shen, B.Y. Guo, A.B. Yu, P.R. Austin, and P. Zulli: *Fuel*, 2011, vol. 90, pp. 728–38.
40. Y.S. Shen, B.Y. Guo, A.B. Yu, and P. Zulli: *ISIJ Int.*, 2009, vol. 49, pp. 819–26.
41. B.Y. Guo, P. Zulli, M. Daniel, A.B. Yu, and Y.S. Shen: *J. Iron. Steel Res. Int.*, 2009, vol. 16, pp. 851–56.
42. B.Y. Guo, Y.S. Shen, A.B. Yu, and P. Zulli: *Proc. 6th Int. Sympos. Multiphase Flow, Heat Mass Transfer and Energy Conversion*, Xi'an Jiaotong University, Xi'an, China, 2009, MN17.
43. C.K. Ho, S.M. Wu, H.P. Zhu, A.B. Yu, and S.T. Tsai: *Miner. Eng.*, 2009, vol. 22, pp. 986–94.
44. H. Nogami, M.S. Chu, and J. Yagi: *Comput. Chem. Eng.*, 2005, vol. 29, pp. 2438–48.
45. Y.S. Shen, A.B. Yu, P.R. Austin, and P. Zulli: *Miner. Eng.*, 2012, vol. 33, pp. 54–65.
46. Y.S. Shen, A.B. Yu, P.R. Austin, and P. Zulli: *Powder Technol.*, 2012, vol. 223, pp. 27–38.
47. W. Ranz and W. Marshall: *Chem. Eng. Prog.*, 1952, vol. 48, pp. 142–80.
48. M. Hatano, T. Miyazaki, and Y. Iwanaga: *Trans. Iron Steel Inst. Jpn.*, 1980, vol. 20, pp. 292–300.